Springer

Acta Mechanica Sinica

CrossMark click for updates

• RESEARCH PAPER •

Acta Mech. Sin., Vol. 40, 323381 (2024)
https://doi.org/10.1007/s10409-023-23381-x

Application of the EA model to the velocity transversal space-time cross-correlation functions measured in the ocean

Changrong Liang[1], Xiaodong Shang[1*], Guiying Chen[1], Xiaozhou He[2*], and Penger Tong[3]

[1] *State Key Laboratory of Tropical Oceanography, South China Sea Institute of Oceanology, Chinese Academy of Sciences, Guangzhou 510301, China;*

[2] *School of Mechanical Engineering and Automation, Harbin Institute of Technology (Shenzhen), Shenzhen 518055, China;*

[3] *Department of Physics, Hong Kong University of Science and Technology, Hong Kong, China*

Received August 11, 2023; accepted August 23, 2023; published online February 7, 2024

The elliptical approximation (EA) model is an important method for deducing spatial fluctuations from the temporal fluctuations at a single point. It has been extensively examined and used in shear fields of desktop experiments for the longitudinal space-time cross-correlation functions $C(r,\tau)$. Here we examine the EA model in the flow field of the ocean and present its application to the transversal space-time cross-correlation functions $G(r,\tau)$. The result shows that EA model is valid for the velocity field of the ocean, that is, $G(r,\tau)$ has the scaling form of $G(r_E,0)$ with $r_E=\left[(r-U\tau)^2+(V\tau)^2\right]^{1/2}$, where U and V are the velocities associated with the vertical phase velocities of the internal waves. Based on the EA model, we can obtain the vertical wavenumber energy spectrum of the ocean and estimate the transversal Taylor micro-scale and Reynolds number.

Elliptical approximation model, Spatial fluctuations, Temporal fluctuations, Space-time cross-correlation functions, Taylor micro-scale

Citation: C. Liang, X. Shang, G. Chen, X. He, and P. Tong, Application of the EA model to the velocity transversal space-time cross-correlation functions measured in the ocean, Acta Mech. Sin. 40, 323381 (2024), https://doi.org/10.1007/s10409-023-23381-x

1. Introduction

Spatial and temporal structure has become an important method for studying the ocean dynamics [1-3]. However, it is difficult to obtain the spatial structure of the flow field in the ocean with current measurement techniques and observation methods. By contrast, we can easily obtain the temporal structure of a fixed point by the method of continuous observation. As a result, to obtain the spatial structure of the flow field, researchers have to rely on Taylor's hypothesis [4], by which the spatial fluctuations can be deduced from the temporal fluctuations measured at a single point. Taylor's hypothesis has been widely used in the ocean. For example, Taylor's hypothesis was used to convert the time series obtained from a submersible particle image velocimetry (PIV) system into spatial series to extend the wavenumber space of spectra [5]. Taylor's hypothesis was employed to convert the acoustic Doppler velocimeter (ADV) velocity measurements into a wavenumber spectrum to estimate the dissipation rate [6]. Taylor's hypothesis was used to convert frequency spectra into wavenumber spectra to study the horizontal distribution of eddy energy and explore the turbulent mixing [7,8]. However, Taylor's hypothesis remains controversial because it heavily relies on the existence of a large mean flow [9,10]. Soloviev and Lukas [10] suggested that the validation of Taylor's hypothesis requires the mean flow to be at least 10 times greater than the perturbation velocity. In flow field with a mean flow smaller than the perturbation velocity, spatial structure derived from Taylor's hypothesis would be erroneous [11,12].

In 2006, He and Zhang [13] introduced an elliptical approximation (EA) model by which they could also deduce the spatial fluctuations from the temporal fluctuations

*Corresponding authors. E-mail addresses: xdshang@scsio.ac.cn (Xiaodong Shang); hexiaozhou@hit.edu.cn (Xiaozhou He)
Executive Editor: Guowei He

measured at a single point. EA model overcomes the weakness of Taylor's hypothesis and can be applied to flow fields without large mean flow. Desktop experiments and numerical simulations have been conducted to assess the ability of EA model to convert temporal statistical quantities into spatial statistical quantities [14]. For example, EA model was verified with direct numerical simulation of turbulent channel flows [15]. EA model was assessed in the temperature and velocity fields of the turbulent Rayleigh-Bénard convection [16-19]. However, as far as we know, no studies have evaluated the EA model in the ocean or applied it to the ocean dynamics. The flow field of the ocean contains various motions, such as internal waves, mesoscale eddies, and circulations [20-23]. It remains unclear whether the EA model is effective in the ocean. Previous desktop experiments and numerical simulations have examined its application to the longitudinal space-time cross-correlation functions. Different from previous studies, here we assess the EA model using the flow field of the ocean and present its application to the transversal space-time cross-correlation functions. This assessment provides reference and evidence for the application of the EA model to the flow field of the ocean, which is important to explore the ocean dynamics.

2. Observations

In 2008, we deployed a mooring over the continental shelf in the northern South China Sea (SCS) (22.15°N, 115.60°W) where the depth of the seabed is 67 m (Fig. 1(a)). The mooring consists of an upward looking 300-kHz acoustic Doppler current profiler (ADCP) at 60 m. Velocity data between 4 and 56 m was collected by the ADCP, which has 2 m vertical resolution and 1 minute temporal resolution. Approximately 16 days data were collected (12:09, Jul 1, 2008 to 03:19, Jul 17, 2008). Figure 1(b) shows the averaged zonal velocity $\overline{u}$ during the observation and the corresponding shear S. $\overline{u}$ decreases almost linearly with increasing depth, which suggests nearly homogeneous shear in the flow. The magnitude of shear in the water column was approximately 6×10^{-3} s^{-1}.

The northern SCS is one of the most active areas in the world, with large amplitude internal waves propagating from the Luzon Strait to the continental shelf [20,24]. Figure 2(a) shows the spectra of the horizontal kinetic energy at mooring site. Significant peaks appear in inertial (f), diurnal (O_1 and K_1), semidiurnal (M_2 and S_2), and higher tidal harmonic (e.g., D3 and D4) frequency bands. Harmonic analysis is performed on the velocity data at each depth to investigate the amplitude and phase of the internal tides [25]. Four (O_1, K_1, M_2, and S_2) primary internal tidal ellipses are shown in Fig. 2(b). The elliptical polarization of the internal tides O_1, K_1, M_2, and S_2 is rotated clockwise, which is consistent with that of freely propagating waves in the northern hemisphere. O_1 and K_1 tidal currents are dominated by baroclinic component, with large variation (Greenwich phase and ellipse inclination) across the water column. M_2

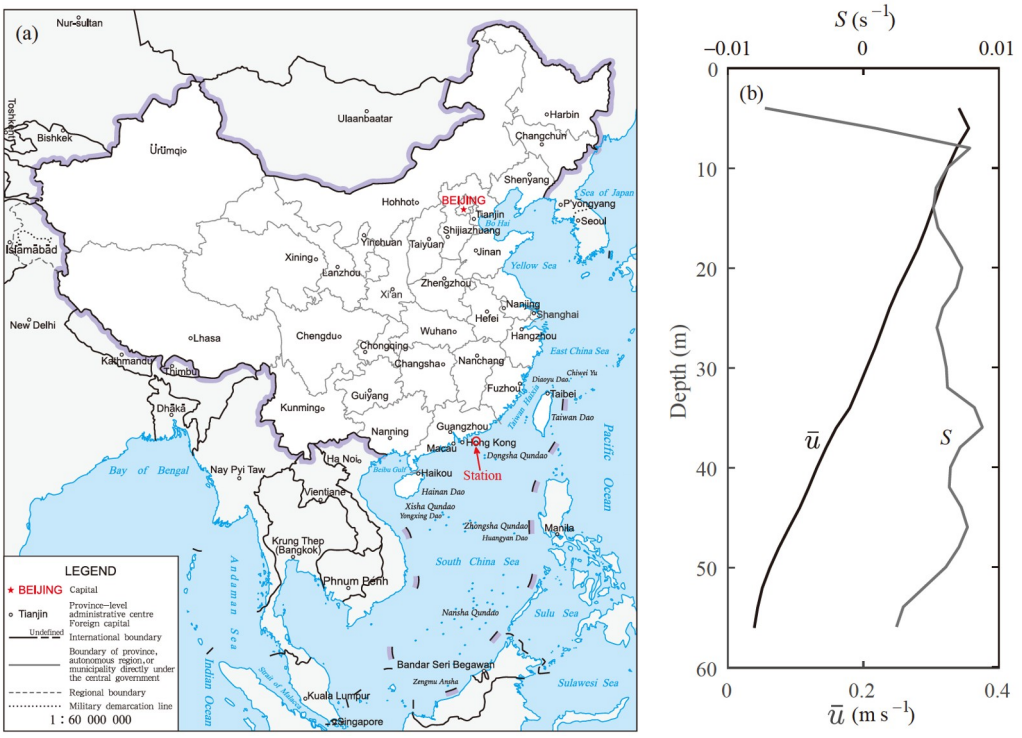

Figure 1 (a) Map showing the observation station (red circle) in the SCS. (b) Profiles of the averaged zonal velocity and the corresponding shear S at the mooring site. The background map is available for download at http://bzdt.ch.mnr.gov.cn/index.html. The drawing review number of the map is GS(2019)1652.

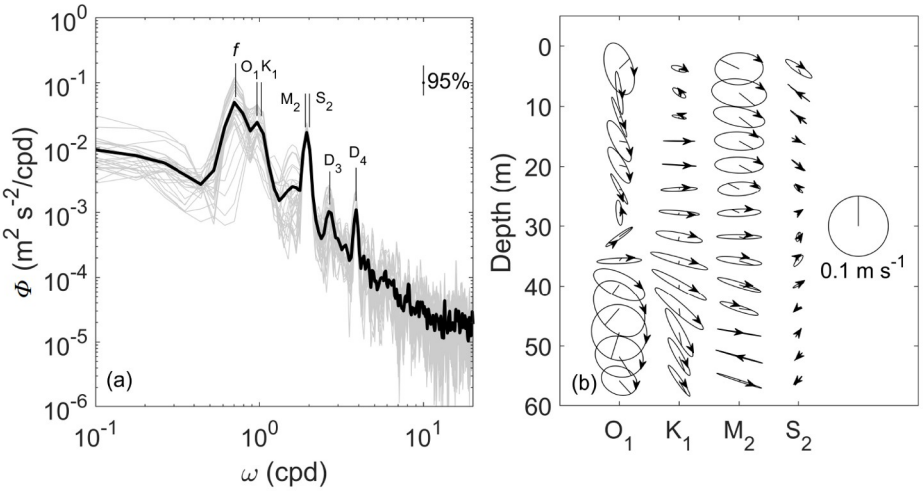

Figure 2 (a) Spectra of horizontal kinetic energy as a function of frequency for all depths (gray). The black curve represents their averaged spectrum. Inertial (f), diurnal (O_1 and K_1), semidiurnal (M_2 and S_2), and high harmonic (D_3 and D_4) frequencies are indicated by vertical lines. The statistical significance level (95%) is indicated by the vertical line. (b) The diurnal (O_1 and K_1) and semidiurnal (M_2 and S_2) measured horizontal current ellipses. The Greenwich phase is denoted by the line within the ellipse, and the direction of rotation of the current is denoted by the arrow. The unit "cpd" means cycle per day.

tidal currents are barotropic, with little variation (Greenwich phase and ellipse inclination) across the water column. S_2 tidal currents are small compared to other tidal currents. The dominant baroclinic component in O_1 and K_1 tidal currents suggests that their vertical phase velocities are relatively small, while strong barotropic component in M_2 tidal currents suggests that M_2 tidal currents have fast vertical phase velocity. In addition to internal waves with tidal frequencies (O_1, K_1, M_2, and S_2), internal waves with other frequencies (e.g., f, D_3, and D_4) also have vertical phase velocities that vary with frequency. Measuring the phase velocities of internal waves and their averaged phase velocity is important to explore the energy cascade among internal waves [26,27].

3. Results

Space-time cross-correlations are the quantities that are commonly used to study the space-time statistics of turbulent flows [28,29]. The velocity transversal space-time cross-correlation function at z_0 is defined as

$$G(r,\tau)=\frac{\langle u(z_0,t)u(z_0+r,t+\tau)\rangle}{\sigma_u(z_0)\sigma_u(z_0+r)}, \tag{1}$$

where $u(z_0,t)$ is the local velocity along the zonal direction, $\sigma_u(z_0)$ is the r.m.s velocity, r is the spatial separation along the vertical direction, τ is the delay time, and $\langle\rangle$ denotes a time average. Near the origin, the cross-correlation function can be expanded using Taylor's series up to the second order:

$$\begin{aligned}G(r,\tau)=&G(0,0)+\frac{\partial G(0,0)}{\partial r}r+\frac{\partial G(0,0)}{\partial \tau}\tau\\&+\frac{1}{2}\frac{\partial^2 G(0,0)}{\partial r^2}r^2+\frac{\partial^2 G(0,0)}{\partial r\partial\tau}r\tau+\frac{1}{2}\frac{\partial^2 G(0,0)}{\partial \tau^2}\tau^2.\end{aligned} \tag{2}$$

In Eq. (2), we have $\partial G(0,0)/\partial\tau=0$ for steady-state flow. While in the shear flow (Fig. 1(b)), we have

$$\begin{aligned}\frac{\partial G(0,0)}{\partial r}&=\frac{\partial\langle u(z_0,t)u(z_0,t)\rangle}{\partial r}\frac{1}{\sigma_u(z_0)\sigma_u(z_0)}\\&=2\left\langle\frac{u(z_0,t)\partial u(z_0,t)}{\partial r}\right\rangle\frac{1}{\sigma_u^2(z_0)}\\&=2\frac{\langle u(z_0,t)\rangle}{\sigma_u^2(z_0)}S.\end{aligned} \tag{3}$$

With Eqs. (2) and (3), we get

$$\begin{aligned}\widetilde{G}(r,\tau)&=G(r,\tau)-2\frac{\langle u(z_0,t)\rangle}{\sigma_u^2(z_0)}S\\&=G(0,0)+\frac{1}{2}\frac{\partial^2 G(0,0)}{\partial r^2}r^2+\frac{\partial^2 G(0,0)}{\partial r\partial\tau}r\tau\\&\quad+\frac{1}{2}\frac{\partial^2 G(0,0)}{\partial\tau^2}\tau^2.\end{aligned} \tag{4}$$

In the r-τ plane, the iso-correlation contours of $\widetilde{G}(r,\tau)$ are a set of self-similar elliptical curves. According to the EA model, one can find a new length scale r_E that satisfies

$$r_E^2=(r-U\tau)^2+(V\tau)^2, \tag{5}$$

and

$$\widetilde{G}(r_E,0)=\widetilde{G}(r,\tau), \tag{6}$$

with

$$U=-\frac{\partial^2 G(0,0)}{\partial r\partial\tau}\left[\frac{\partial^2 G(0,0)}{\partial r^2}\right]^{-1}, \tag{7}$$

and

$$V^2=\frac{\partial^2 G(0,0)}{\partial\tau^2}\left[\frac{\partial^2 G(0,0)}{\partial r^2}\right]^{-1}-U. \tag{8}$$

Equation (5) is the EA model introduced by He and Zhang

[13]. EA model is a plausible extension of Taylor's hypothesis to the flow fields without large mean flow. It becomes Taylor's hypothesis when V vanishes, $r_T = r - U\tau$.

In Eq. (4), $2\frac{\langle u(z_0,t)\rangle}{\sigma_u^2(z_0)}S$ can be ignored if S is infinitely close to zero, in which case, $G(r,\tau) \cong \widetilde{G}(r,\tau)$ and EA model can also be applied to $G(r,\tau)$. Next, we assess the application of EA model to $G(r,\tau)$ using the velocity $u(z,t)$ measured in the ocean. Figure 3 shows the flood contours of the measured $G(r,\tau)$ as a function of r and τ at z_0 = 30 m. As expected, $G(r,\tau)$ is a single peaked function with a maximal value at the origin $(r,\tau) = (0, 0)$ and decays to negative value at large r or τ. $G(r,\tau)$ decays slowly along the preferential direction (the major axis of ellipse), and decays quickly in the direction perpendicular to the preferential direction. If Taylor's hypothesis holds for the present flow field, the iso-correlation contours of $G(r,\tau)$ should be degenerated to straight lines, $r_T = r - U\tau$. However, the iso-correlation contours of $G(r,\tau)$ are significantly different from the straight lines predicted by Taylor's hypothesis. They are more like the elliptic curves that can be described by the elliptic forms, $r_E^2 = (r-U\tau)^2 + (V\tau)^2$, defined from EA model. This suggests that EA model works better than Taylor's hypothesis in the present flow field. However, the iso-correlation contours gradually deform as r or τ increase. Only iso-correlation contours at r < 5 m can be well described by the elliptic forms while those at r > 5 m deviate from the elliptic forms (comparing with the cyan dashed elliptic curves in Fig. 3). This deviation mainly results from the term $\frac{\partial G(0,0)}{\partial r}r$ in Eq. (2). This term depends on $\frac{\langle u(z_0,t)\rangle}{\sigma_u^2(z_0)}$ and S (see Eq. (3)). In the observed flow field, S is not zero

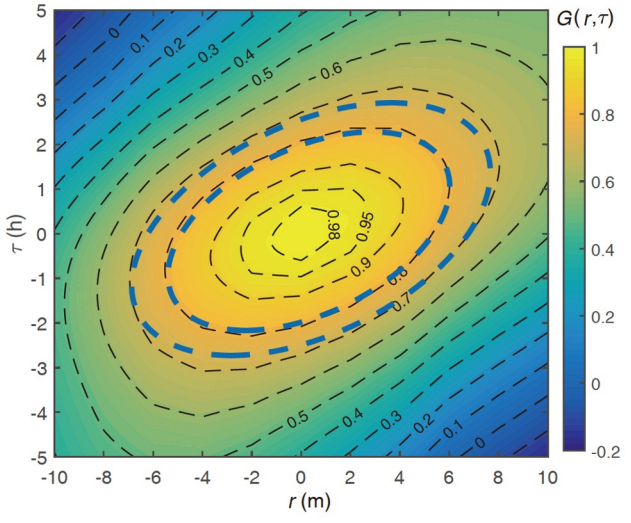

Figure 3 Velocity transversal space-time cross-correlations $G(r,\tau)$ vs. r and τ at z_0 = 30 m. The cyan dashed curves show ellipses for comparison.

(Fig. 1(b)). The effect of $\frac{\partial G(0,0)}{\partial r}r$ can't be ignored at large r, which leads to the iso-correlation contours deviate from the elliptic forms at large r (> 5 m).

To verify the EA model, we need to obtain the two velocities U and V in Eq. (5). According to He et al.'s [16] inference, $G(r_E,0)$ is a decreasing function of r_E in which a minimum r_E will correspond to a maximum $G(r_E,0)$; thus, the peak positions r_p and τ_p at which the correlation function reaches its maximum can be determined by the conditions that $\partial r_E/\partial r\,|_\tau = 0$ and $\partial r_E/\partial \tau\,|_r = 0$, respectively, from which we can obtain

$$r_p = U\tau, \tag{9}$$

and

$$\tau_p = \frac{U}{\left(U^2+V^2\right)}r. \tag{10}$$

It is observed from Fig. 3 that $G(r,\tau)$ at a fixed $\tau(r)$ is a single peaked function with peak position $r_p(\tau_p)$. In other words, r_p is the only spatial separation that maximizes $G(r,\tau)$ at a fixed τ and τ_p is the only time delay that maximizes $G(r,\tau)$ at a fixed r. Thus, r_p and τ_p can also be directly determined by the iso-correlation contours of $G(r,\tau)$. Figure 4(a) and (b) shows r_p as a function of τ and τ_p as a function of r, respectively. If the EA model is applicable to all τ and r, r_p will be a linear function of τ, as in Eq. (9), and τ_p will be a linear function of r, as in Eq. (10). However, r_p shows a linear function of τ only at $\tau \in [-2.5\ 2.5]$ h and τ_p shows a linear function of r only at $r \in [-5\ 5]$ m. Deviations from the linear functions at $|\tau|$ > 2.5 h and $|r|$ > 5 m are mainly due to the deformation of ellipses caused by $\frac{\partial G(0,0)}{\partial r}r$. Therefore, only data at $\tau \in [-2.5\ \ 2.5]$ h and $r \in [-5\ 5]$ m are used to determine their linear functions, respectively. The result shows that $r_p = \alpha_0\tau$ with α_0 = 1.06 m h^{-1} and $\tau_p = \beta_0 r$ with β_0 = 0.15 h m^{-1}. Combining $r_p = \alpha_0\tau$ and $\tau_p = \beta_0 r$ with Eqs. (9) and (10) gives

$$U = \alpha_0, \tag{11}$$

and

$$\frac{U}{U^2+V^2} = \beta_0. \tag{12}$$

Solving Eqs. (11) and (12), we obtain U = 1.06 m h^{-1} and V = 2.4378 m h^{-1}.

Next, we assess the relation between $G(r,\tau)$ and $G(r_E,0)$ with the obtained U and V. Figure 4(c) shows the evolution of $G(r,\tau)$ versus the delay time τ for several different spatial separations. These correlation curves initially increase to the maximum and then decrease. Every curve has a single peak at τ_p and gradually becomes asymmetric as r increases.

Figure 4(d) shows the evolution of $G(r,\tau)$ versus $r_E=[(r-U\tau)^2+(V\tau)^2]^{1/2}$ defined from EA model, with U = 1.06 m h^{-1} and V = 2.4378 m h^{-1}. For comparison, the directly measured $G(r,0)$ is also plotted as a function of r in Fig. 4(d) (open circles). The measured correlation curves collapse on top of each other and match the directly measured $G(r,0)$ at r_E < 5 m, indicating that the measured $G(r,\tau)$ have the predicted scaling form $G(r_E,0)$ and EA model holds for r_E < 5 m. However, correlation curves gradually deviate from each other at r_E > 5 m. These deviations mainly result from the non-zero term $\frac{\partial G(0,0)}{\partial r}=2\frac{\langle u(z_0,t)\rangle}{\sigma_u^2(z_0)}S$. Shear determines the degree of deviation of the curve. The greater the shear is, the faster the curve deviates. In our observation, correlation curves collapse into a single master curve at r_E < 5 m, which indicates that the effect of $\frac{\partial G(0,0)}{\partial r}$ on the application of EA model can be ignored at r_E < 5 m.

An important application of the EA model in the ocean is to obtain wavenumber spectrum from time series data. One implication of EA model is that when r = 0, we have $G(0,\tau)=G(r_E,0)$. Therefore, $G(0,\tau)$ can be directly used to evaluate $G(r_E,0)$ and its vertical wavenumber energy spectrum $E(k_z)$. Figure 5(a) shows the measured $E(k_z)$ at z = 30 m based on EA model. Note that the energy spectrum is only valid at k_z > 1/5 m^{-1} because the EA model only holds for r_E < 5 m. Here we designate the minimum effective wavenumber as k_{z1}, k_{z1} = 0.2 m^{-1}, and the maximum effective wavenumber as k_{z2}, k_{z2} = 6.3 m^{-1}. k_{z2} is the maximum wavenumber not effected by vibration noise. Two distinct subranges of length scales can be identified in the effective wavenumber range [k_{z1} k_{z2}]. One subrange (0.2 < k_z < 2) contains motions with length scale between 0.5 and 5 m. Energy in this subrange decays slowly, with a power law of $k_z^{-0.2}$. Another subrange (2 < k_z < 6.3) contains motions with length scale between 0.16 and 0.5 m. Energy decays rapidly in this subrange, with a power law of $k_z^{-2.5}$.

Another important application of EA model is to estimate the transversal Taylor micro-scale λ_g. λ_g is defined by [30]

$$\lambda_g(t)=\left[-\frac{1}{2}G''(0,t)\right]^{-1/2}, \tag{13}$$

where $G''(0,t)=(\partial^2G/\partial^2r)_{r=0}$. Letting $p(r)$ be the parabola osculating $G(r)$ at r = 0, i.e., $p(0)=G(0)$, $p'(0)=G'(0)$, and $p''(0)=G''(0)$, we obtain

$$p(r)=1+\frac{1}{2}G''(0)r^2=1-\frac{r^2}{\lambda_g^2}. \tag{14}$$

For small values of r, $G(r,\tau)\simeq p(r)$ [13,15,16]. Thus, we

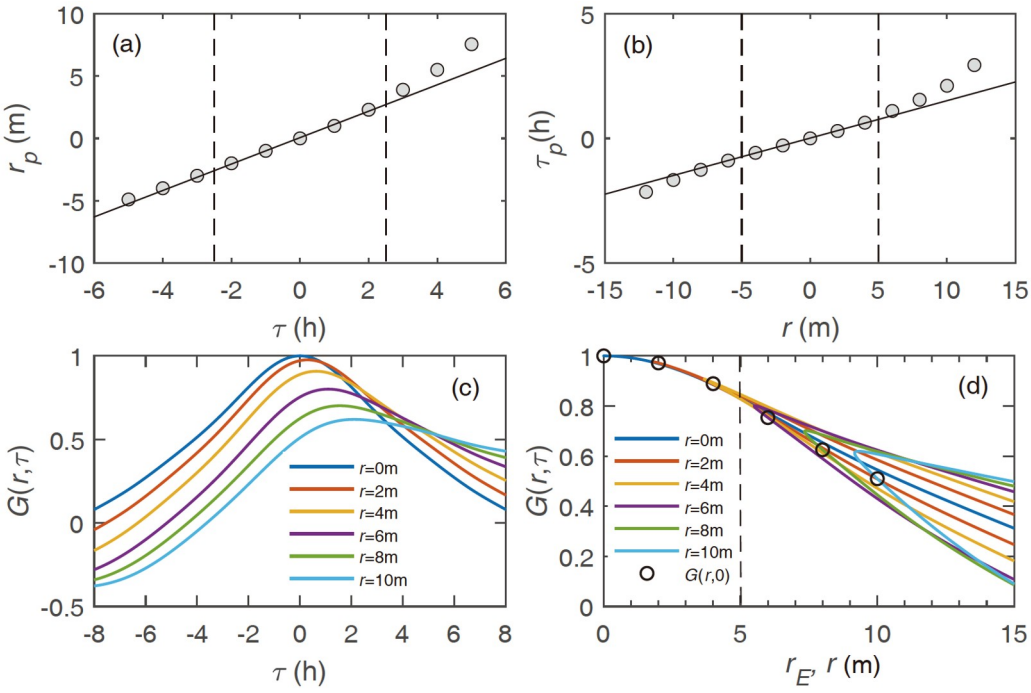

Figure 4 (a) The measured r_p vs. τ. $r_p=\alpha_0\tau$ based on data between the two vertical dashed lines is shown by the solid line. (b) The measured τ_p vs. r. $\tau_p=\beta_0 r$ based on data between the two vertical dashed lines is showed by the solid line. Velocity transversal space-time cross-correlations $G(r,\tau)$ for several different spatial separations (r = 0 m, 2 m, 4 m, 6 m, 8 m, and 10 m) are plotted vs. (a) τ and (b) $r_E=[(r-U\tau)^2+(V\tau)^2]^{1/2}$ defined from EA model. The measured $G(r,0)$ vs. r is shown by the open circles. The vertical dashed line in (d) indicates the distance at which the cross-correlations $G(r,\tau)$ begin to deviate from each other.

have

$$\lambda_g \simeq \frac{r}{\sqrt{1-G(r,0)}} \tag{15}$$

for small values of r. Figure 5(b) shows $\lambda_E = r_E/\sqrt{1-G(r_E,0)}$ as a function of r_E, where $G(r_E,0)$ is obtained from $G(0,\tau)$ based on the EA model. The directly measured $\lambda(r) = r/\sqrt{1-G(r,0)}$ (circles) was also plotted in Fig. 5(b) for comparison. The obtained $\lambda(r_E)$ are in agreement with the measured $\lambda(r)$, especially at the distance ($r_E < 5$ m) at which EA model is valid. We obtain $\lambda_g \simeq \lambda(r_E) \simeq 11.2$ m for small r_E. The Reynolds number based on the transversal Taylor microscale is $Re_{\lambda_g} \simeq \left(U^2+V^2\right)^{1/2}\lambda_g/\nu \simeq 8845$, where $\nu = 9.35\times10^{-7}$ m^2 s^{-1} is the kinematic viscosity of seawater.

Based on the EA model, we also obtain two characteristic velocities U and V. These two velocities are associated with the vertical phase velocities of the internal waves. The observed flow field contains internal waves of various frequencies, which propagate downward or upward at different vertical phase velocities in the water column. The propagation properties of internal waves make the velocity signals at different depths correlated with each other. Yet, more observations and numerical simulations are needed to study the effects of internal waves with different phase velocities on U and V, and the EA model in the near future.

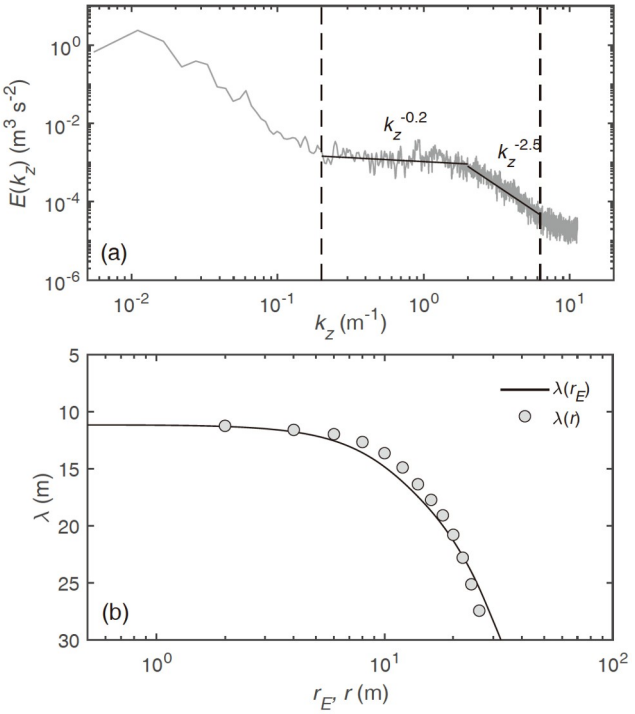

Figure 5 (a) Velocity energy spectrum $E(k_z)$ vs. k_z. The vertical dashed lines indicate the lower limit k_{z1} and the upper limit k_{z2} of the effective wavenumbers. The solid lines indicate the power laws $E(k_z) \sim k_z^{-0.2}$ and $E(k_z) \sim k_z^{-2.5}$. (b) Length scale $\lambda_E = r_E/\sqrt{1-G(r_E,0)}$ as a function of r_E obtained from the EA model (curve). Directly measured $\lambda(r) = r/\sqrt{1-G(r,0)}$ vs. r is shown by the circles.

4. Conclusions

We have presented a systematic investigation of the application of the EA model to the velocity transversal space-time cross-correlation functions $G(r,\tau)$ of the velocity field over the continental shelf in the northern SCS. The result shows that the iso-correlation contours of $G(r,\tau)$ have an elliptical curve shape. With the separation r_E defined from the EA model to scale $G(r,\tau)$, the correlation curves collapse into a single master curve at $r < 5$ m. The correlation curves at $r > 5$ m fail to collapse on top of each other. Failure of the EA model at large separation mainly results from the non-zero $\partial G(0,0)/\partial r$ which depends on shear. Previous studies have verified that EA model is suitable for longitudinal space-time cross-correlation functions in desktop experiments [16,17,19]. In this study, we first verify that EA model is also suitable for the transversal space-time cross-correlation functions in the ocean. Based on the EA model, we can obtain the vertical wavenumber energy spectrum of the ocean using time series data at a single point, which is difficult to obtain by direct observation. We can also estimate the transversal Taylor micro-scale and Reynolds number of the ocean. These physical quantities are essential for understanding the ocean dynamics.

Conflict of interest *On behalf of all authors, the corresponding author states that there is no conflict of interest.*

Author contributions *Xiaodong Shang and Guiying Chen formulated the overarching research goals, designed the research, and administered the project. Changrong Liang supervised the research activity, conducted the research and investigation process, and wrote the first draft of the manuscript. Xiaozhou He, Penger Tong, and Xiaodong Shang analyzed or synthesized study data, and revised and edited the final version.*

Acknowledgements *This work was supported by the National Key Research and Development Program of China (Grant No. 2021YFC3101300), the innovation project of Innovative Academy of Marine Information Technology, Chinese Academy of Sciences (Grant No. CXBS202101), the National Natural Science Foundation of China (Grant Nos. 41876022, 12372216, 41630970, and 41806033), the Science, Technology and Innovation Commission of Shenzhen Municipality (Grant No. GXWD20220818113020001), and the Science and Technology Program of Guangzhou (Grant No. 202102020707). The numerical simulation was supported by the High Performance Computing Division and HPC managers of Wei Zhou and Dandan Sui in the South China Sea Institute of Oceanology.*

1 D. Dommenget, An objective analysis of the observed spatial structure of the tropical Indian Ocean SST variability, Clim. Dyn. **36**, 2129 (2011).
2 G. C. Johnson, E. Kunze, K. E. McTaggart, and D. W. Moore, Temporal and spatial structure of the equatorial deep jets in the pacific ocean, J. Phys. Oceanogr. **32**, 3396 (2002).
3 Y. D. Resnyanskii, M. D. Tsyrulnikov, B. S. Strukov, and A.

A. Zelenko, Statistical structure of spatial variability of the ocean thermohaline fields from argo profiling data, 2005-2007, Oceanology **50**, 149 (2010).
4 G. I. Taylor, The spectrum of turbulence, Proc. R. Soc. Lond. A **164**, 476 (1938).
5 P. Doron, L. Bertuccioli, J. Katz, and T. R. Osborn, Turbulence characteristics and dissipation estimates in the coastal ocean bottom boundary layer from PIV data, J. Phys. Oceanogr. **31**, 2108 (2001).
6 R. C. Lien, and E. A. D'Asaro, Measurement of turbulent kinetic energy dissipation rate with a lagrangian float, J. Atmos. Ocean. Tech. **23**, 964 (2006).
7 P. Bouruet-Aubertot, H. van Haren, and M. P. Lelong, Stratified inertial subrange inferred from *in situ* measurements in the bottom boundary layer of the rockall channel, J. Phys. Oceanography **40**, 2401 (2010).
8 R. Ferrari, and C. Wunsch, The distribution of eddy kinetic and potential energies in the global ocean, TELLUSA **62**, 92 (2010).
9 A. Bahraminasab, M. D. Niry, J. Davoudi, M. Reza Rahimi Tabar, A. A. Masoudi, and K. R. Sreenivasan, Taylor's frozen-flow hypothesis in Burgers turbulence, Phys. Rev. E **77**, 065302 (2008).
10 A. Soloviev, and R. Lukas, Observation of wave-enhanced turbulence in the near-surface layer of the ocean during TOGA COARE, Deep Sea Res. Part I-Oceanographic Res. Papers **50**, 371 (2003).
11 T. M. Dillon, and D. R. Caldwell, The Batchelor spectrum and dissipation in the upper ocean, J. Geophys. Res. **85**, 1910 (1980).
12 J. L. Lumley, Interpretation of time spectra measured in high-intensity shear flows, Phys. Fluids **8**, 1056 (1965).
13 G. W. He, and J. B. Zhang, Elliptic model for space-time correlations in turbulent shear flows, Phys. Rev. E **73**, 055303 (2006).
14 G. He, G. Jin, and Y. Yang, Space-time correlations and dynamic coupling in turbulent flows, Annu. Rev. Fluid Mech. **49**, 51 (2017).
15 X. Zhao, and G. W. He, Space-time correlations of fluctuating velocities in turbulent shear flows, Phys. Rev. E **79**, 046316 (2009).
16 X. He, G. He, and P. Tong, Small-scale turbulent fluctuations beyond Taylor's frozen-flow hypothesis, Phys. Rev. E **81**, 065303 (2010).
17 X. He, and P. Tong, Kraichnan's random sweeping hypothesis in homogeneous turbulent convection, Phys. Rev. E **83**, 037302 (2011).
18 X. He, D. P. M. van Gils, E. Bodenschatz, and G. Ahlers, Reynolds numbers and the elliptic approximation near the ultimate state of turbulent Rayleigh-Bénard convection, New J. Phys. **17**, 063028 (2015).
19 Q. Zhou, C. M. Li, Z. M. Lu, and Y. L. Liu, Experimental investigation of longitudinal space-time correlations of the velocity field in turbulent Rayleigh-Bénard convection, J. Fluid Mech. **683**, 94 (2011).
20 M. H. Alford, T. Peacock, J. A. MacKinnon, J. D. Nash, M. C. Buijsman, L. R. Centurioni, S. Y. Chao, M. H. Chang, D. M. Farmer, O. B. Fringer, K. H. Fu, P. C. Gallacher, H. C. Graber, K. R. Helfrich, S. M. Jachec, C. R. Jackson, J. M. Klymak, D. S. Ko, S. Jan, T. M. S. Johnston, S. Legg, I. H. Lee, R. C. Lien, M. J. Mercier, J. N. Moum, R. Musgrave, J. H. Park, A. I. Pickering, R. Pinkel, L. Rainville, S. R. Ramp, D. L. Rudnick, S. Sarkar, A. Scotti, H. L. Simmons, L. C. St Laurent, S. K. Venayagamoorthy, Y. H. Wang, J. Wang, Y. J. Yang, T. Paluszkiewicz, and T. Y. (David) Tang, The formation and fate of internal waves in the South China Sea, Nature **521**, 65 (2015).
21 R. Ferrari, and C. Wunsch, Ocean circulation kinetic energy: Reservoirs, sources, and sinks, Annu. Rev. Fluid Mech. **41**, 253 (2009).
22 C. R. Liang, G. Y. Chen, X. D. Shang, X. H. Xie, and D. X. Wang, Observation of enhanced nonlinear interactions after severe tropical storm Chanchu (2004) in the Western South China Sea, JGR Oceans **124**, 3837 (2004).
23 C. Xu, X. D. Shang, and R. X. Huang, Estimate of eddy energy generation/dissipation rate in the world ocean from altimetry data, Ocean Dyn. **61**, 525 (2011).
24 Z. Zhao, Internal tide radiation from the Luzon Strait, JGR Oceans **119**, 5434 (2014).
25 R. Pawlowicz, B. Beardsley, and S. Lentz, Classical tidal harmonic analysis including error estimates in MATLAB using T_TIDE, Comput. Geosci. **28**, 929 (2002).
26 W. H. Munk, Internal waves and small scale processes, in: Evolution of Physical Oceanography (MIT Press, Cambridge, 1981). pp. 264-291.
27 A. Tabaei, T. R. Akylas, and K. G. Lamb, Nonlinear effects in reflecting and colliding internal wave beams, J. Fluid Mech. **526**, 217 (2005).
28 M. J. Lighthill, On sound generated aerodynamically, I. General theory, Proc. R. Soc. Lond. A **211**, 564 (1952).
29 C. Meneveau, and J. Katz, Scale-invariance and turbulence models for large-eddy simulation, Annu. Rev. Fluid Mech. **32**, 1 (2000).
30 S. B. Pope, Turbulent Flows (Cambridge University Press, Cambridge, 2000). pp. 91-95.

EA模型在海洋的速度横向时空互相关函数中的应用

梁长荣, 尚晓东, 陈桂英, 何晓舟, 童彭尔

摘要 椭圆近似(EA)模型是从单个点的时间波动数据中推断空间波动数据的重要方法, 它已在室内实验剪切场的纵向时空互相关函数$C(r,\tau)$得到验证并被广泛应用. 在这里, 我们研究了EA模型在海洋流场中的有效性, 并介绍了其在横向时空互相关函数$G(r,\tau)$中的应用. 结果表明, EA模型在海洋的速度场中是有效的, 即$G(r,\tau)$具有$G(r_E,0)$的尺度形式, 其中$r_E=[(r-U\tau)^2+(V\tau)^2]^{1/2}$, U和V是与内波垂直相速度相关的两个特征速度. 基于EA模型, 我们可以获得海洋的垂直波数能谱, 并估计海洋的泰勒微尺度和雷诺数.